Check for updates

ADVANCED MATERIALS
www.advmat.de

Embedded Skyrmion Bags in Thin Films of Chiral Magnets

Luyan Yang, Andrii S. Savchenko, Fengshan Zheng,* Nikolai S. Kiselev,* Filipp N. Rybakov, Xiaodong Han, Stefan Blügel, and Rafal E. Dunin-Borkowski*

Magnetic skyrmions are topologically nontrivial spin configurations that possess particle-like properties. Earlier research has mainly focused on a specific type of skyrmion with topological charge $Q = -1$. However, theoretical analyses of 2D chiral magnets have predicted the existence of skyrmion bags—solitons with arbitrary positive or negative topological charge. Although such spin textures are metastable states, recent experimental observations have confirmed the stability of isolated skyrmion bags in a limited range of applied magnetic fields. Here, by utilizing Lorentz transmission electron microscopy, the extraordinary stability of skyrmion bags in thin plates of B20-type FeGe is shown. In particular, it is shown that skyrmion bags embedded within a skyrmion lattice remain stable even in zero or inverted external magnetic fields. A robust protocol for nucleating such embedded skyrmion bags is provided. The results agree perfectly with micromagnetic simulations and establish thin plates of cubic chiral magnets as a powerful platform for exploring a broad spectrum of topological magnetic solitons.

1. Introduction

Topological magnetic solitons[1] are stable configurations of magnetization fields that are characterized by nontrivial topology. Similar to classical particles or particles in high energy physics, topological magnetic solitons can move and interact with each other in response to external stimuli, e.g., magnetic field,[2,3] temperature,[4–6] and electric current.[7–9] While experiments are typically carried out on 3D samples of magnetic crystals, most of the magnetic solitons that have been observed belong to the class of 2D topological solitons.[10,11] The corresponding magnetic configurations are therefore only localized in two spatial dimensions, usually in the plane of the sample. In the third dimension, they extend through the sample to its physical edges. In chiral magnets, an elementary 2D topological soliton represents a vortex-like texture, in which the magnetization twists by π from its center to its periphery, as shown in the inset of **Figure 1a**. In bulk samples, such textures extend through the full sample thickness and are referred to as skyrmions. It is common to refer to such filamentary magnetic textures as skyrmion strings.[12–15] The magnetic textures of such strings in any plane parallel to the sample surfaces are equivalent to each other up to trivial transformations.

For magnetic textures that are localized in 2D, the classifying group is the second homotopy group of the two-sphere. This group is isomorphic to the group of integers with respect to

L. Yang, X. Han
Beijing Key Laboratory of Microstructure and Property of Advanced Materials
College of Materials Science and Engineering
Beijing University of Technology
Beijing 100124, China

L. Yang, R. E. Dunin-Borkowski
Ernst Ruska-Centre for Microscopy and Spectroscopy with Electrons
Forschungszentrum Jülich
52425 Jülich, Germany

A. S. Savchenko, N. S. Kiselev, S. Blügel
Peter Grünberg Institute
Forschungszentrum Jülich and JARA
52425 Jülich, Germany
E-mail: a.savchenko@fz-juelich.de; n.kiselev@fz-juelich.de

The ORCID identification number(s) for the author(s) of this article can be found under https://doi.org/10.1002/adma.202403274

© 2024 The Author(s). Advanced Materials published by Wiley-VCH GmbH. This is an open access article under the terms of the Creative Commons Attribution-NonCommercial-NoDerivs License, which permits use and distribution in any medium, provided the original work is properly cited, the use is non-commercial and no modifications or adaptations are made.

DOI: 10.1002/adma.202403274

F. Zheng
Spin-X Institute, Center for Electron Microscopy
School of Physics and Optoelectronics
State Key Laboratory of Luminescent Materials and Devices
Guangdong-Hong Kong-Macao Joint Laboratory of Optoelectronic and Magnetic Functional Materials
South China University of Technology
Guangzhou 511442, China
E-mail: zhengfs@scut.edu.cn

F. N. Rybakov
Department of Physics and Astronomy
Uppsala University
Box-516, Uppsala SE-751 20, Sweden

X. Han
Department of Materials Science and Engineering
Southern University of Science and Technology
Shenzhen 518055, China

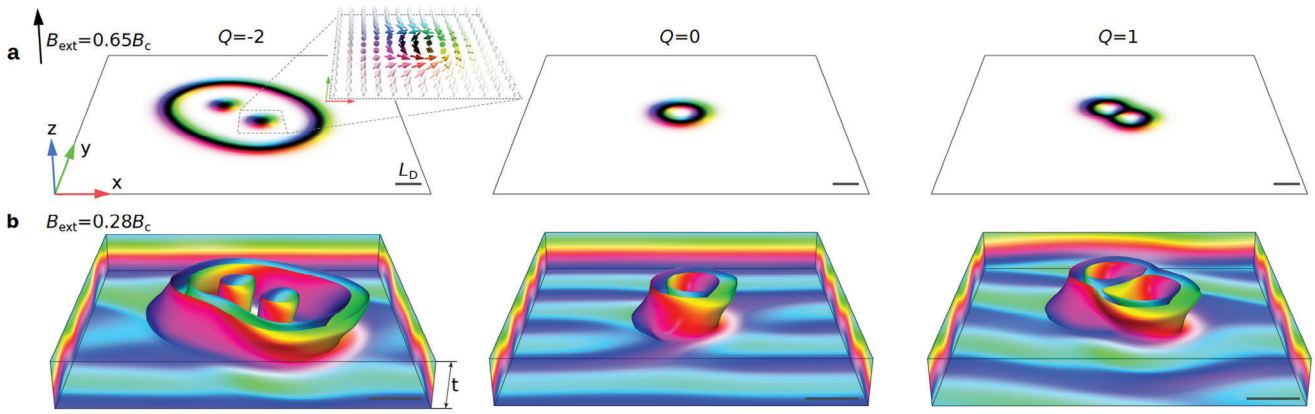

Figure 1. Skyrmions of arbitrary topological charge in the 2D model and in a film of an isotropic chiral magnet. Horizontal panels (a) and (b) show representative skyrmion bags with topological charges $Q = -2$, 0, and 1. a) illustrates skyrmion bags in a 2D system. The magnetization field direction is depicted by means of a standard color code in all of the images, as explained in the inset. Panel (b) illustrates skyrmion bags in a 3D system. The plate thickness t is close to an equilibrium period of the chiral modulation L_D ($t = 0.85L_D$). The magnetization field in (b) is visualized in the form of isosurfaces of $m_z = 0$ and magnetization at the boundaries of the simulated domain. Demagnetizing fields are taken into account for a plate of finite thickness in (b) and are omitted for the 2D system in (a). In both cases, the external magnetic field B_{ext} is perpendicular to the film. Its magnitude is given with respect to the critical field B_c. See the Experimental Section for details. The scale bar in all images corresponds to 1 L_D. Figure S1 (Supporting Information) shows an extended version of this figure that includes the case of a thick film.

addition: $\pi_2(\mathbb{S}^2, \mathbf{m}_0) = \mathbb{Z}$, where $\mathbf{m}_0$ is the base point.[16] A localized continuous magnetic texture can thereby be attributed to an integer number, which is usually termed the skyrmion topological charge and can be calculated using the following invariant:

$$Q = \frac{1}{4\pi}\int_{\Omega} \mathbf{m}\cdot\left[\partial_x\mathbf{m}\times\partial_y\mathbf{m}\right]\mathrm{d}x\mathrm{d}y \tag{1}$$

where $\mathbf{m}(x, y) = \mathbf{M}/|\mathbf{M}|$ is the unit vector field of magnetization and Ω is the skyrmion localization area, such that at its boundary $\partial\Omega$ the magnetization field $\mathbf{m}(\partial\Omega) = \mathbf{m}_0$. Following the standard convention, the right-handed Cartesian coordinate system xyz is chosen so that $\mathbf{m}_0 \cdot \mathbf{e}_z > 0$. For additional details, see Ref. [17].

Two magnetic textures with the same topological charge are topologically equivalent, meaning that they can be transformed continuously into each other. Moreover, magnetic configurations with $Q \neq 0$ cannot be transformed continuously into a ferromagnetic state without the formation of singularities, which are typically associated with high-energy states, suggesting that the decay of a topological soliton requires an energy barrier to be overcome. The experimentally observed collapse and nucleation of skyrmions indicate that, at certain conditions, the system can overcome this energy barrier.[18] Thereby, the stability of magnetic solitons, besides the above topological arguments, is also determined by the interplay of competing magnetic interactions.

Here, we study magnetic skyrmions in thin plates of isotropic chiral magnets that are stabilized by a competition between Heisenberg ferromagnetic exchange and the chiral Dzyaloshinskii–Moriya interaction (DMI),[19,20] in the presence of external magnetic fields applied perpendicular to the plates.

Axially symmetric solutions, or so-called $k\pi$-skyrmions,[21,22] are known to have topological charges of $Q = 0$ for even k and $Q = -1$ for odd k. In these structures, as one moves from the periphery to the center of the vortex, the magnetization rotates by $k\pi$, where k is an integer. For example, an ordinary skyrmion with $Q = -1$ is sometimes referred to as a π-skyrmion, while the skyrmionium with $Q = 0$ depicted in the middle panel of Figure 1a is often called a 2π-skyrmion.

Most earlier experimental studies of B20-type crystals of chiral magnets have been devoted to the static, dynamic, and transport properties of π-skyrmions.[2,23,24] However, recent theoretical studies of 2D models of chiral magnets have predicted that there is an infinite diversity of skyrmions with arbitrary positive and negative topological charges.[25,26] We refer to these configurations as "skyrmion bags", following established terminology in the literature.[26–39]

Various aspects of skyrmion bags have been discussed in the literature in recent years. For instance, the diversity of skyrmion bags has been discussed in Refs. [27, 28], skyrmion bag dynamics induced by electric currents, voltages, and other stimuli have been studied in Refs. [29–34] and skyrmion bag response to time-dependent external magnetic fields has been studied in Refs. [35–40].

We recall that the ground state of an isotropic chiral magnet is a homochiral spin spiral.[41] In the absence of an external magnetic field, this spiral has a period $L_D = 4\pi\mathcal{A}/\mathcal{D}$, which is defined by the ratio of the Heisenberg exchange stiffness $\mathcal{A}$ and the DMI constant $\mathcal{D}$. In these systems, skyrmion bags can be stabilized by the external magnetic field. Representative examples of skyrmion bags with $Q = -2$, 0, and 1 in a 2D system are shown in Figure 1a. Figure 1b shows skyrmion bags with the same topological charges obtained as stable solutions in a 3D system, in which the plate thickness t is assumed to be close to the period of the helical modulations L_D. Details about the model and micromagnetic simulations are given in the Experimental Section. Due to the isotropic properties of ferromagnetic exchange and DMI, these magnetic configurations show additional modulations along the thickness of the plate. As a result, the isosurfaces of the skyrmion bags show distortions and twists along the z-axis.

© 2024 The Author(s). Advanced Materials published by Wiley-VCH GmbH

15214095, 2024, 36, Downloaded from https://onlinelibrary.wiley.com/doi/10.1002/adma.202403274 by Forschungszentrum Jülich GmbH Research Center, Wiley Online Library on [02/10/2024]. See the Terms and Conditions (https://onlinelibrary.wiley.com/terms-and-conditions) on Wiley Online Library for rules of use; OA articles are governed by the applicable Creative Commons License

The magnetization field around a skyrmion bag is not a ferromagnetic state with $\mathbf{m}\|\mathbf{e}_z$, as in the 2D case. Instead, here, the magnetization field takes the form of a conical spin spiral, whose k-vector is parallel to the external magnetic field $\mathbf{B}_{ext}$. As the topological charge remains fixed in any xy-plane, such configurations can be identified as quasi-2D skyrmion bags.

Experimental observations and current-driven motion of skyrmion bags with positive topological charge $0 \leq Q \leq 52$ were recently reported in chiral magnets and referred to as *skyrmion bundles*.[42,43] The topologically trivial soliton with $Q = 0$ depicted in the central column of Figure 1 was also observed experimentally earlier.[42,44,45] Recently, skyrmion bags of diverse topological charge were also reported in van der Waals ferromagnets,[46] where they were referred to as *composite skyrmions* and in hexaferrite.[47] However, the observation of skyrmion bags with negative topological charges in chiral magnets has proved to be more challenging. It was recently shown that in thick films of an isotropic chiral magnet with $t \gtrsim 2L_D$, the outer rings of skyrmion bags tend to transform into hopfion rings.[17] Moreover, in Ref. [17], it was shown that 3D magnetic textures should be characterized by a more general homotopy group, in which the corresponding invariant is defined by the *skyrmion–hopfion* topological charge represented by a pair of integers (Q, H). Formally, magnetic configurations with ($Q \neq 0$, $H = 0$) should be attributed to 2D topological solitons, whereas configurations with (Q, $H \neq 0$) should be attributed to 3D topological solitons. Representative examples of skyrmion bags shown in Figure 1 belong to the class of 2D topological solitons. The outer ring of a skyrmion bag with $Q = -2$ shown in Figure 1b can only transform into a hopfion ring in a relatively thick film (Figure S1, Supporting Information). Therefore, a plate with a thickness in the range $0 < t \lesssim L_D$ is more suitable for the observation of skyrmion bags with negative topological charge (for B20-type FeGe, $L_D = 70$ nm). The fabrication of such plates with a thickness below 100 nm using the standard method of focused ion beam milling is challenging.

In the present work, we describe the experimental observation of magnetic skyrmion bags with negative topological charges embedded in a skyrmion lattice in a 70-nm-thick FeGe plate. We also provide a reliable approach for their nucleation, based on the experimental diagram of magnetic states in such a thin sample explored in our earlier study.[45]

2. Results

2.1. Micromagnetic Simulations

Figure 2 shows micromagnetic simulations, which demonstrate that the range of external magnetic fields in which isolated skyrmion bags remain stable is relatively narrow. When B_{ext} is reduced below ≈120 mT, the isolated skyrmion bags exhibit an instability with respect to elongation (Figure S2a–c, Supporting Information). When B_{ext} is increased above 340 mT, the isolated skyrmion bags become unstable with respect to topological transitions. In our simulations, configurations with $Q = 0$ and 1 transform into chiral bobbers (Figure S2d, Supporting Information), whereas skyrmion bags with $Q = -2$ transform into pairs of skyrmions through the collapse of their outer rings (Figure S2e, Supporting Information).

In contrast, we find that skyrmion bags that are embedded in skyrmion lattices remain stable over very wide ranges of applied fields, even when the directions of these fields are inverted. In our calculations, we assume periodic boundary conditions in the plane of the plate and an extended system with a fixed skyrmion density of ≈150 μm^{-2}, in order to approximate the samples of confined geometry that are used in our experiments. Our results show that a variation in skyrmion density does not change the skyrmion bag stability range significantly. Most importantly, the embedded skyrmion bags remain stable even in negative fields of up to $B_{ext} = -240$ mT. For $B_{ext} < -240$ mT, even though the structure of the skyrmion lattice undergoes irreversible changes, the skyrmion bags can still be identified when the magnetic field is switched back to the positive direction. As a result, even $B_{ext} = -240$ mT is not a strict critical field for embedded skyrmions, but can be regarded as an approximate lower bound. Such extraordinary stability makes embedded skyrmion bags more accessible for experimental observations when compared to isolated skyrmion bags.

In positive fields, the embedded skyrmion bags exhibit an instability at nearly the same field of ≈350 mT as isolated skyrmion bags. In our micromagnetic simulations, at $B_{ext} > 320$ mT a skyrmion bag with $Q = 1$ transitions into a skyrmionium with $Q = 0$, which itself transforms into an ordinary skyrmion with $Q = -1$ at $B_{ext} > 350$ mT. The skyrmion bag with $Q = -2$ turns out to be the most stable solution, which then collapses into an ordinary skyrmion at $B_{ext} > 400$ mT. Although the energies of the skyrmion bags are provided in Figure 2c to illustrate the difference in the stability range between isolated and embedded skyrmion bags, it should be noted that a direct comparison of energies may be misleading since the backgrounds for isolated and embedded skyrmions are different.

Figure 2d illustrates the energy dependence of isolated and embedded skyrmion bags as a function of plate thickness. The fact that the self-energies of skyrmion bags increase with the thickness also suggests that thin film is more optimal for skyrmion bag observation. The non-monotonic character of the energy dependence of isolated skyrmion bags (open circles) is because according to our observations the surface modulations which are well-seen in Figure 1b (see stripe-like pattern) show a tendency to be most pronounced only for thicknesses commensurate to a half period of the equilibrium chiral modulations, $t = \frac{1}{2}nL_D$, where n is integer. On the contrary, for $t = \frac{1}{2}nL_D \pm \frac{1}{4}L_D$, we observe that surface modulations become energetically unfavorable and disappear. Such an intriguing behavior is observed for all thicknesses $t \leq 2L_D$ and fixed applied magnetic field. It is also worth noting that at the chosen field strength of 200 mT, the isolated skyrmion bags become unstable when the plate thickness, t, is reduced below $0.75L_D$, whereas this is not the case for embedded skyrmion bags.

2.2. Experimental Stability Diagram of Magnetic States in a Thin FeGe Plate

We studied a thin FeGe plate with a lateral dimension of 1×1 μm and a nominal thickness of 70 nm, which corresponds to $1L_D$. This sample was used in our previous work,[45] where we estimated the stability diagram of magnetic states, which is

© 2024 The Author(s). Advanced Materials published by Wiley-VCH GmbH

15214095, 2024, 36, Downloaded from https://onlinelibrary.wiley.com/doi/10.1002/adma.202403274 by Forschungszentrum Jülich GmbH Research Center, Wiley Online Library on [02/10/2024]. See the Terms and Conditions (https://onlinelibrary.wiley.com/terms-and-conditions) on Wiley Online Library for rules of use; OA articles are governed by the applicable Creative Commons License

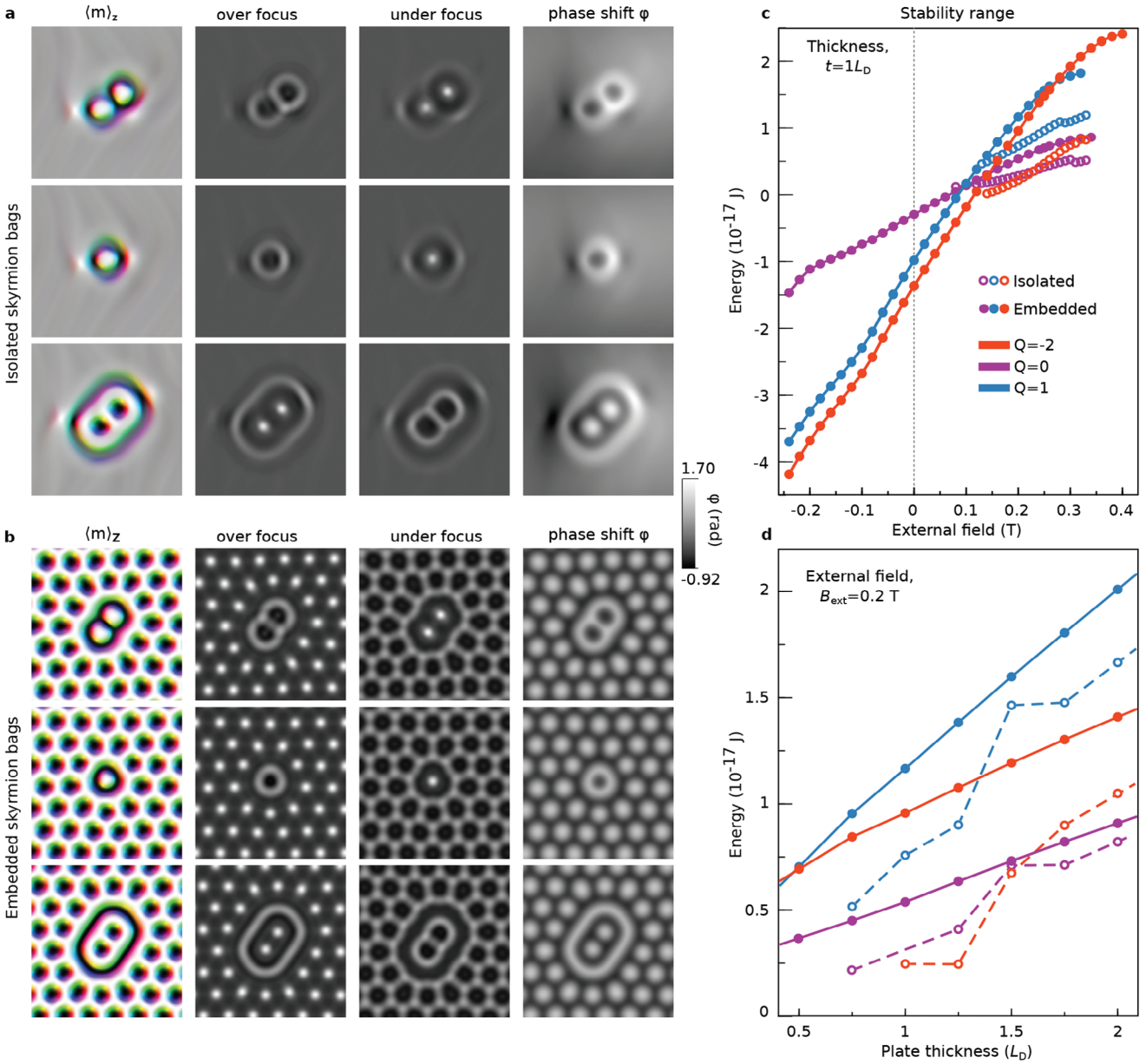

Figure 2. Micromagnetic simulations of isolated and embedded skyrmion bags. Panel (a) shows solutions for isolated skyrmion bags, while Panel (b) shows skyrmion bags embedded in skyrmion lattices at $B_{ext} = 200$ mT. The simulations were performed on a large domain of 1.05 × 1.04 μm with periodic boundary conditions. The images in panels (a) and (b) have identical sizes of 525 × 520 nm and show only the central region of the simulated domain. The first column shows the magnetization field averaged over the thickness of the plate for skyrmion bags with $Q = -2$, 0 and 1, as shown in Figure 1b. Here, we use a specific color code,[48] with convergence to a gray color when $|\langle \mathbf{m} \rangle_z| \to 0$. The second and third columns show corresponding calculated over-focus and under-focus Lorentz TEM images. The defocus distance is 800 μm. The fourth column shows the calculated phase shift, φ, which would be recorded using off-axis electron holography. All phase shift images are shown on the same scale. Panel (c) plots the energies of isolated and embedded skyrmion bags as a function of the perpendicular applied magnetic field for the plate of thickness $t = 1L_D$. Panel (d) shows the energies of isolated and embedded skyrmion bags as a function of plate thickness at a fixed magnetic field of 200 mT. The energies of the isolated solutions are given with respect to the energy of the conical phase, while the energies of the embedded solutions are given with respect to the energy of a regular skyrmion lattice. The isolated skyrmion bags remain stable over a finite range of fields applied in a positive direction only. The embedded skyrmion bags are stable over a wider range of applied fields, including inverted fields. The isolated skyrmion bags in Panel (d) also exhibit elliptic instability at a thickness of below $0.75L_D$, while embedded skyrmion bags remain stable with decreasing thickness. The energies of isolated and embedded skyrmion bags increase with plate thickness.

© 2024 The Author(s). Advanced Materials published by Wiley-VCH GmbH

15214095, 2024, 36, Downloaded from https://onlinelibrary.wiley.com/doi/10.1002/adma.202403274 by Forschungszentrum Jülich GmbH Research Center, Wiley Online Library on [02/10/2024]. See the Terms and Conditions (https://onlinelibrary.wiley.com/terms-and-conditions) on Wiley Online Library for rules of use; OA articles are governed by the applicable Creative Commons License

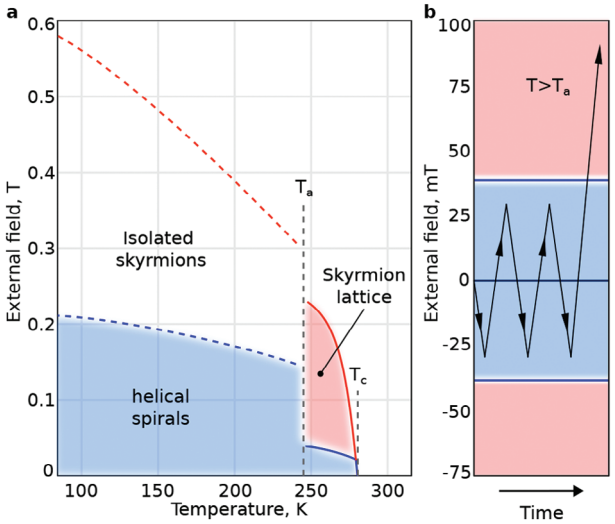

Figure 3. Temperature—applied magnetic field diagram of magnetic states in a 70-nm-thick FeGe plate. Panel (a) shows a diagram of magnetic states observed with increasing external magnetic field reproduced using data from Ref. [45], which were measured by in situ Lorentz TEM experiments. We estimate the activation temperature $T_a = 245$ K and the critical temperature $T_c = 278$ K. For $T < T_a$, the dashed blue line marks the instability of the helical spin spiral state with respect to a transition to individual skyrmions. The dashed red line corresponds to the collapse of skyrmions. For $T_a < T < T_c$, the solid blue line marks an abrupt transition between a helical spin spiral state and a regular skyrmion lattice. The solid red line corresponds to the nearly simultaneous collapse of all skyrmions. Panel (b) shows a schematic representation of our embedded skyrmion bag nucleation protocol at $T > T_a$. We first apply several cycles of a lower field between negative and positive directions. The applied field is then gradually increased above a value that induces a transition from helical spin spirals to a skyrmion lattice.

reproduced in **Figure 3**a. The blue and red dashed lines were estimated at increasing magnetic fields. Below the dashed lines, one can observe either isolated skyrmions or helical spirals.

The diagram shows that when the temperature increases above the so-called activation temperature T_a, the system undergoes an abrupt transition into a skyrmion lattice phase. This transition can be induced by varying the applied magnetic field or temperature. At a sample temperature in the range $T_a \lesssim T \lesssim T_c$ and an external field in the range 40 mT $\lesssim B_{ext} \lesssim$ 220 mT, we always observe the appearance of a skyrmion lattice. The protocol for the nucleation of embedded skyrmion bags that we introduce below relies on the abrupt transition between helical spirals and a skyrmion lattice induced by an external magnetic field.

2.3. Protocol for Skyrmion Bag Nucleation

Figure 4 shows a sequence of over-focus Lorentz TEM images, which illustrate a protocol for the reliable nucleation of skyrmion bags. The images were recorded at a sample temperature of $T =$ 250 K, which is above the activation temperature. At this temperature, the transition into a skyrmion lattice occurs at ≈39 mT. The magnitude of the magnetic field applied in the positive and negative directions should therefore be lower than this value. We estimated the optimal magnitude of the magnetic field to be $\lesssim$ 30 mT.

We start from a helical spiral state in zero magnetic field at a temperature of $T > T_a$, as shown in Figure 4a. We first apply a few cycles of varying magnetic field, that is always oriented perpendicular to the plate but changes in direction from positive to negative, as shown schematically in Figure 3b. The aim of this step is to create closed loops of helical spin spirals. Figure 4c–e shows the formation of helical spirals (marked by red lines) near the edges, while two helical spirals (marked by yellow lines) in the interior of the sample form a closed loop after the first and second field swapping cycles. A skyrmion bag with $Q = -1$ is embedded in the helical spirals. We then increase the field gradually to induce a transition from the helical spirals to a skyrmion lattice state, as shown in Figure 4h–j.

With more field-swapping cycles, we observe that closed loops can also be formed from the edges, leading to a diversity of skyrmion bags embedded in the helical spirals and skyrmion lattice. In this way, the number of skyrmions inside the bag and the number of closed loops can be controlled. Furthermore, the initial configuration of the system influences the diversity of the skyrmion bags. For instance, Figure S3 (Supporting Information) illustrates the above protocol for an initial configuration of an ideal helical spin spiral. This protocol is conceptually identical to that used for the nucleation of skyrmion–antiskyrmion pairs[45] and hopfion rings.[17] However, here, we apply it at elevated temperatures.

The lateral size of the sample is a critical factor for the effectiveness of this protocol. We suppose that the dimensions used in our experiment (1 × 1 μm) are close-to-optimal. We tested a larger sample (3 × 3 μm) and observed that the protocol was not as effective as for the smaller sample. In particular, we encountered difficulties achieving a coherent appearance of the edge modulations around the sample perimeter. We attribute this effect to minor variations in thickness, which become more pronounced with increasing sample size.

2.4. Diversity of Embedded Skyrmion Bags

By following the above protocol, we obtained a wide diversity of skyrmion bags embedded in skyrmion lattices. Representative examples of skyrmion bags with different topological charges are shown in **Figure 5**. Further examples of negative skyrmion bags are provided in Figure S5 (Supporting Information).

Positive skyrmion bags with $Q > 0$ embedded in a skyrmion lattice were not observed in our experiments. Instead, we observed such skyrmion bags embedded in helical spirals (see Figure S11, Supporting Information). Alternative protocols based on the use of ultrashort energy pulses, such as those from electric currents or ultrafast lasers, may be helpful to nucleate positive skyrmion bags embedded in skyrmion lattices.

Merging of skyrmion bags was also not observed. Even when there were several skyrmion bags in the system, as shown in Figure 5b,d,h, we never observed the merging of their outer rings.

The shape and position of a skyrmion bag were found to depend not only on the number of field-swapping cycles but also on the angle of the applied magnetic field. In general, the use of a tilted magnetic field breaks the symmetry of the system by making specific directions of magnetization in the plane more favorable than others, resulting in an obstacle to the formation

© 2024 The Author(s). Advanced Materials published by Wiley-VCH GmbH

15214095, 2024, 36, Downloaded from https://onlinelibrary.wiley.com/doi/10.1002/adma.202403274 by Forschungszentrum Jülich GmbH Research Center, Wiley Online Library on [02/10/2024]. See the Terms and Conditions (https://onlinelibrary.wiley.com/terms-and-conditions) on Wiley Online Library for rules of use; OA articles are governed by the applicable Creative Commons License

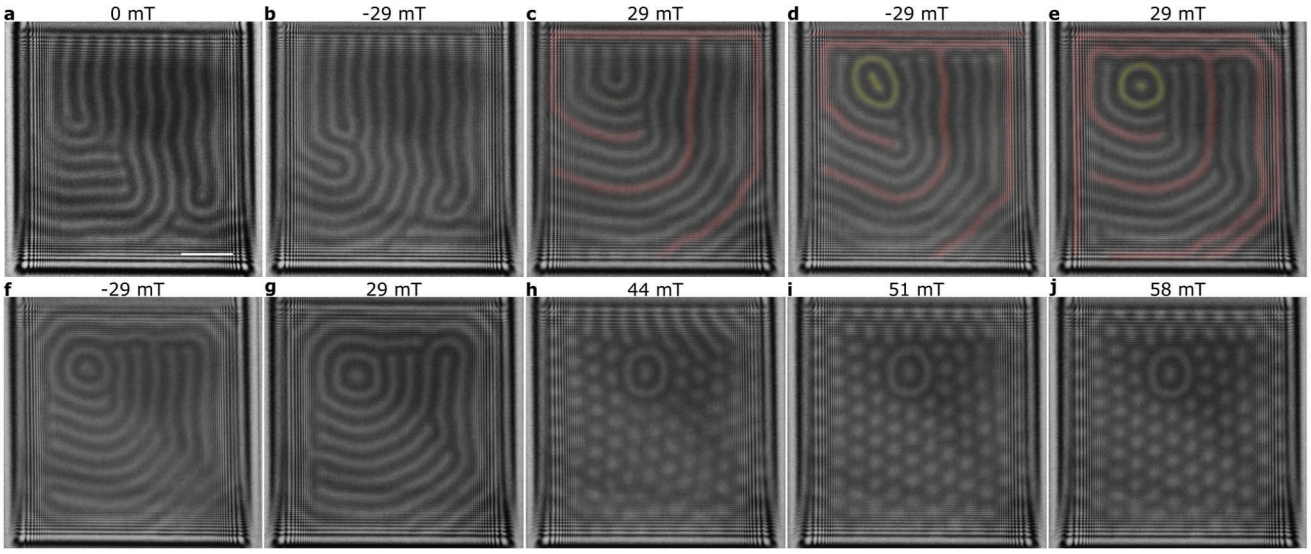

Figure 4. Nucleation protocol for skyrmion bags in a 70-nm-thick FeGe plate. Panel (a) shows a random initial magnetic state in zero magnetic field. We chose a magnetic field of ≈30 mT for the field-swapping process. Panels (b,c) show states in the first swapping cycle between −29 and +29 mT. Panel (c) shows the formation of a helical spiral near the edge (red line). Two short spirals (yellow lines) are pushed and turned into a skyrmion bag, with a skyrmion inside them in the second cycle, as shown in (d) and (e). The skyrmion bag is located in the background of the helical spirals, with a topological charge of −1. Two further helical modulations are created continuously from the edge of the sample with more cycles of field swapping, as shown in (d,e) and (f,g). By following the red line, these newly formed helical spirals are pushed gradually toward the inner area of the sample. On increasing the field further, such helical spirals transition into skyrmions, resulting in skyrmion bags embedded in the skyrmion lattice, as shown in (h–j). The frames show over-focus Lorentz TEM images recorded at $T = 250$ K. The defocus distance is 800 µm. The value of the applied magnetic field is indicated above each frame. The scale bar in (a) is 200 nm. Figure S3 (Supporting Information) shows another example of skyrmion bag nucleation in the sample. Figure S9 (Supporting Information) shows skyrmion bag nucleation in a 180-nm-thick FeGe plate.

of closed loops of helical spirals from the sample edges. The tilt angle of the magnetic field was, therefore, always kept below 5° in our experiments.

2.5. Skyrmion Bags in Inverted Magnetic Fields

In order to verify the prediction of the micromagnetic model about the stability of skyrmion bags in inverted magnetic fields, we performed dedicated experiments at reduced temperature, since the micromagnetic constants used in the simulations were adapted for the low-temperature regime. We first nucleated skyrmion bags by following the above protocol at a higher temperature of 250 K and then cooled the sample to 95 K. Representative examples of the field evolution of skyrmion bags with topological charges of $Q = 0$, −1, and −2 in negative fields are shown in Figures S6–S8 (Supporting Information), respectively. All of the skyrmion bags exhibit topological instability in applied magnetic fields of between −150 and −200 mT but are otherwise in good agreement with the micromagnetic simulations shown in Figure 2c, in which skyrmion bags embedded in a skyrmion lattice are shown to be stable over a wide range of external magnetic fields in both directions. This slight discrepancy between theory and experiment can be attributed to the confined sample geometry and to the fact that thermal fluctuations are ignored in the micromagnetic simulations.

An intriguing asymmetry is observed in the contrast of the skyrmions, especially in strong negative fields, in Figures S6–S8 (Supporting Information). Remarkably, similar contrast was recently observed in the $Fe_{0.5}Co_{0.5}Ge$ helimagnet.[49] This behavior resembles an initial stage of a process that is referred to as *turning a skyrmion inside out*,[50] in which a skyrmion gradually transforms into an antiskyrmion.[45] With increasing negative field, the number of spins pointing along the field increases gradually. The negative direction then takes over the role of the base point $\mathbf{m}_0$, which, in turn, leads to a flip of the coordinate system in Equation (1). A dedicated discussion of this intriguing transformation will be presented elsewhere.

3. Discussion

In order to distinguish the observed skyrmion bags from hopfion rings, we performed quantitative measurements using off-axis electron holography, as shown in **Figure 6**. The skyrmions and the outer rings of the skyrmion bags produced nearly identical recorded phase shifts, confirming that the rings penetrate through the thickness of the plate. In contrast, the signal from a hopfion ring depicted in Figure S12 (Supporting Information) is significantly weaker, in agreement with experimental observations.[17]

The protocol presented here only allows skyrmion bags embedded in a skyrmion lattice to be nucleated in very thin films of FeGe. We attempted to reproduce the protocol in a 180-nm-thick FeGe plate of identical lateral size (1 × 1 µm). Snapshots of the system during field swapping cycles are provided in Figure S9 (Supporting Information). Over seven cycles, helical spirals from the edges (marked in red) propagated gradually to the center of the sample and finally formed a single skyrmion. This final

© 2024 The Author(s). Advanced Materials published by Wiley-VCH GmbH

15214095, 2024, 36, Downloaded from https://onlinelibrary.wiley.com/doi/10.1002/adma.202403274 by Forschungszentrum Jülich GmbH Research Center, Wiley Online Library on [02/10/2024]. See the Terms and Conditions (https://onlinelibrary.wiley.com/terms-and-conditions) on Wiley Online Library for rules of use; OA articles are governed by the applicable Creative Commons License

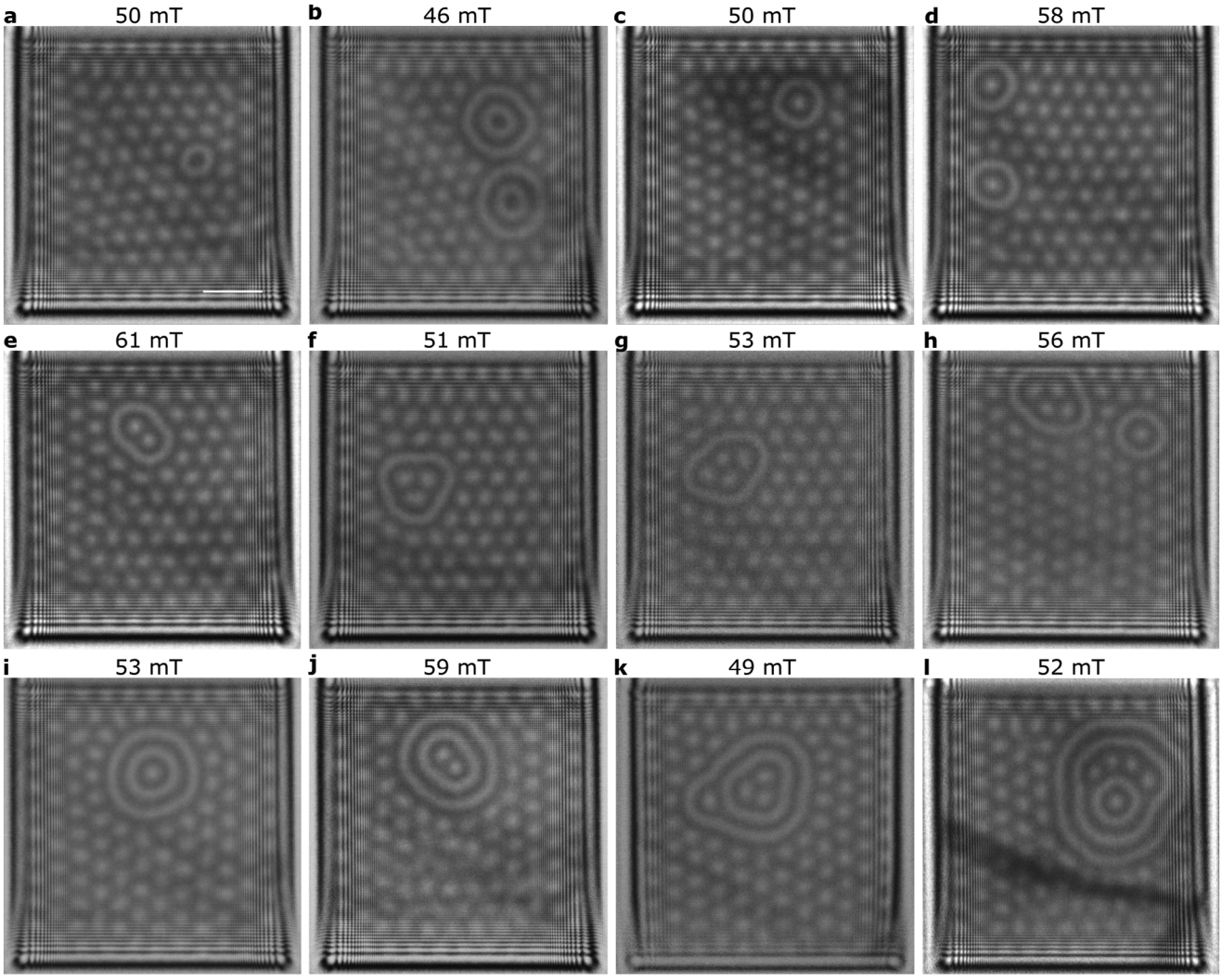

Figure 5. Representative examples of skyrmion bags with negative topological charge in a 70-nm-thick FeGe plate. Panel (a) shows a single embedded skyrmionium. Panel (b) shows two so-called 4π-skyrmions with $Q = 0$. Panel (c) shows a single 3π-skyrmion, i.e., a skyrmion bag with $Q = -1$. Panel (d) shows a pair of 3π-skyrmions. Panels (e–g) show embedded skyrmions with two, three and four skyrmions inside outer rings and topological charge $Q = -2$, -3 and -4, respectively. Panel (h) shows the coexistence of two skyrmion bags with $Q = -4$ and -1. Panel (i) shows an embedded 5π-skyrmion. Panels (j–l) show non-axially-symmetric skyrmion bags with multiple rings and topological charge $Q = -2$, -4 and -5, respectively. All of the images were recorded over-focus at a temperature of $T = 250$ K at a defocus distance of 800 µm. The scale bar in (a) is 200 nm.

configuration represents a nearly ideal set of nested closed loops of helical spirals. The behavior of the helical spirals nucleating at the edges of thicker and thinner films is, therefore, nearly identical. By following this approach, one can obtain skyrmion bags embedded in the helical spirals, as shown in Figure S10 (Supporting Information). However, on further increasing the applied magnetic field, the texture undergoes a transition to a skyrmion lattice state, including the helical spirals and skyrmion bags. A representative example of such a state, after increasing the field above the transition to a skyrmion lattice, is shown in Figure S10h (Supporting Information). This behavior can be explained by the fact that, in a thick film, a skyrmion bag state is energetically higher than that of a hopfion ring. In order to reduce its energy, the system therefore shrinks any closed ring into a hopfion ring. However, at higher temperature the hopfion ring collapses, leading to a state in which only skyrmions are present.

In conclusion, our results provide direct experimental evidence for the formation of magnetic skyrmion bags embedded in skyrmion lattices or helical spirals in thin plates of B20-type FeGe. Micromagnetic simulations support our observations and show excellent agreement with the experimental results. Magnetic skyrmion bags with tunable topological charge offer a powerful platform to study both the fundamental physics and the dynamical and topological properties of magnetic solitons.

4. Experimental Section

Magnetic Imaging in the TEM: TEM samples were prepared from a single crystal of B20-type FeGe using a focused ion beam workstation and a lift-out method.[51] The nominal sample size was 1×1 µm and the thickness of the sample was ≈70 nm, as determined by measurements from a cross-sectional image obtained using scanning electron microscopy. The

© 2024 The Author(s). Advanced Materials published by Wiley-VCH GmbH

15214095, 2024, 36, Downloaded from https://onlinelibrary.wiley.com/doi/10.1002/adma.202403274 by Forschungszentrum Jülich GmbH Research Center, Wiley Online Library on [02/10/2024]. See the Terms and Conditions (https://onlinelibrary.wiley.com/terms-and-conditions) on Wiley Online Library for rules of use; OA articles are governed by the applicable Creative Commons License

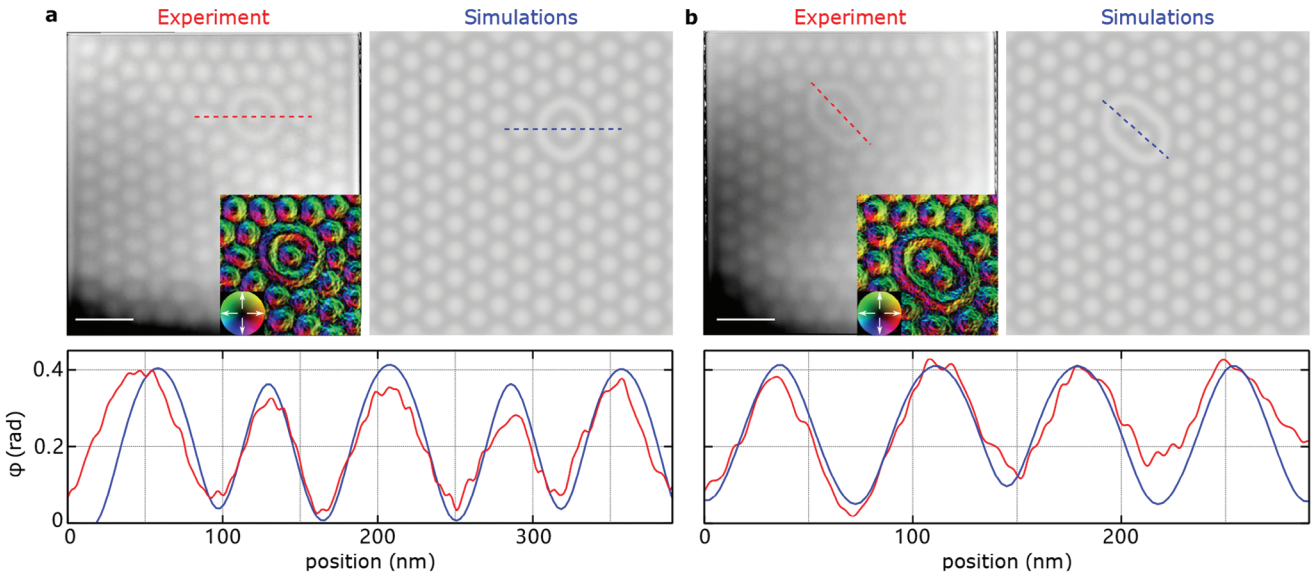

Figure 6. Comparison between experimental and theoretical electron phase shift images of skyrmion bags in a 70-nm-thick FeGe plate. Panel (a) shows an embedded skyrmion bag with $Q = -1$, and panel (b) shows an embedded skyrmion bag with $Q = -2$. Experimental and simulated electron phase shift images are shown on the left and right, respectively. Line profiles taken from the experimental (red) and simulated (blue) images across the center of each skyrmion bag are shown below. Corresponding experimental Lorentz TEM images for the two skyrmion bags are shown in Figure 5c,e, respectively. The insets to the experimental images show the projected magnetic induction field of the corresponding skyrmion bag. In the line profiles, the skyrmions and the outer rings of the skyrmion bags have nearly identical contrast, indicating that the rings, which are composed of two nested 180° domain walls, penetrate the full sample thickness. This behavior is in contrast to that observed for hopfion rings in thicker films (Figure S12, Supporting Information), in which the contrast from the ring is much weaker than that of the individual skyrmions. The experimental images were recorded at $T = 250$ K. The scale bars in (a) and (b) are 200 nm. The micromagnetic model parameters were adapted to this temperature. For details, see the Experimental Section.

crystallographic orientation of the sample was ≈2° from the [110] direction. More details about sample characterization can be found in Ref. [45]. Fresnel defocus imaging and off-axis electron holography were performed at 300 kV in an FEI Titan 60-300 TEM equipped with an electrostatic biprism. Each image was first adjusted to be close to focus, where there was little magnetic contrast. The defocus was tuned to be over-focus or under-focus, in order to obtain visible magnetic contrast. The microscope was operated in Lorentz mode with the sample either in magnetic-field-free conditions or in a pre-calibrated out-of-plane magnetic field applied using the conventional microscope objective lens. A liquid-nitrogen-cooled specimen holder (Gatan model 636) was used to vary the sample temperature between 95 and 380 K. Fresnel defocus images and off-axis electron holograms were recorded using a 4k × 4k Gatan K2 IS direct electron counting detector. Multiple electron holograms, with a 4 s exposure time for each hologram, were recorded to improve the signal-to-noise ratio. Holograms were analyzed using a standard fast Fourier transform algorithm in Holoworks software (Gatan). The magnetic induction maps that are shown in Figure 6 were obtained from the gradients of recorded magnetic phase images.

Micromagnetic Calculations: A micromagnetic model described by the following energy functional was used:[14,52]

$$\mathcal{E} = \int_{V_m} d\mathbf{r}\, \mathcal{A} \sum_{i=x,y,z} |\nabla m_i|^2 + \mathcal{D}\,\mathbf{m}\cdot(\nabla \times \mathbf{m}) - M_s\,\mathbf{m}\cdot\mathbf{B}_{tot} + \frac{1}{2\mu_0}\int_{\mathbb{R}^3} d\mathbf{r} \sum_{i=x,y,z} |\nabla A_{d,i}|^2 \quad (2)$$

where $\mathcal{A}$ and $\mathcal{D}$ are the Heisenberg exchange and DMI constants; μ_0 is the vacuum permeability; $\mathbf{m}(\mathbf{r}) = \mathbf{M}(\mathbf{r})/M_s$ is the unit vector field of the normalized magnetization, M_s is the saturation magnetization, $\mathbf{A}_d(\mathbf{r})$ is the component of the magnetic vector potential induced by the magnetization[52] and V_m is the volume of the calculation domain. The total magnetic field $\mathbf{B}_{tot}$ includes the external magnetic field $\mathbf{B}_{ext}$ and the demagnetizing field produced by the sample,[14,52] according to the expression $\mathbf{B}_{tot} = \mathbf{B}_{ext} + \nabla \times \mathbf{A}_d$. Micromagnetic calculations based on energy minimization to find solutions of Equation (2), as well as simulations of Lorentz TEM images and electron phase shift images, were performed using Excalibur software.[53] Detailed descriptions of the methods are provided in Ref. [14].

Without considering the effect of demagnetizing fields in bulk chiral magnets, the conical phase transitions into the saturated ferromagnetic state above its critical field, $B_c = B_D = \mathcal{D}^2/(2M_s\mathcal{A})$. When taking demagnetizing fields into account, the critical field for cone saturation is given by $B_c = B_D + \mu_0 M_s$.

In order to estimate the stabilities of the skyrmion bags in Figure 2, the following parameters were used for FeGe:[14,45,54] $\mathcal{A} = 4.75$ pJm^{-1}, $\mathcal{D} = 0.853$ mJm^{-2} and $M_s = 384$ kAm^{-1}, resulting in excellent agreement with experimental data recorded at 95 K. The calculation domains had sizes of 1.05 µm × 1.04 µm × 70 nm, on the assumption of periodic boundary conditions in the *xy* plane. The initial state represented a skyrmion bag of given topological charge located approximately in the center of the simulated domain and embedded in the corresponding phase (cone or skyrmion lattice). Such states converged to nearby local energy minima during energy minimization.

For simulations of the electron phase shift images shown in Figure 6, the simulated domain had open boundary conditions in all directions. In order to adapt the micromagnetic model to match the experimental conditions at $T = 250$ K, the following experimental observations were taken into account for FeGe: 1) the equilibrium period of the spin spiral ($L_D = 4\pi\mathcal{A}/\mathcal{D}$) remains fixed with a negligibly small variation of ≈2.8% over the entire temperature range[55,56]; 2) M_s decreases with increasing temperature and, according to Ref. [57], at 240 K it decreases by up to 125 kAm^{-1}. The adapted model maintained fixed values for $\mathcal{A}$ and $\mathcal{D}$, while assuming an approximate value for M_s of 120 kAm^{-1} at $T = 250$ K.

© 2024 The Author(s). Advanced Materials published by Wiley-VCH GmbH

15214095, 2024, 36, Downloaded from https://onlinelibrary.wiley.com/doi/10.1002/adma.202403274 by Forschungszentrum Jülich GmbH Research Center, Wiley Online Library on [02/10/2024]. See the Terms and Conditions (https://onlinelibrary.wiley.com/terms-and-conditions) on Wiley Online Library for rules of use; OA articles are governed by the applicable Creative Commons License

Supporting Information

Supporting Information is available from the Wiley Online Library or from the author.

Acknowledgements

The authors thank Haifeng Du for help with specimen preparation. This project received funding from the European Research Council under the European Union's Horizon 2020 Research and Innovation Programme (Grant No. 856538 - project "3D MAGiC") and the Deutsche Forschungsgemeinschaft (Project-ID 405553726 – TRR 270; Priority Programme SPP 2137; Project No. 403502830). L.Y. acknowledges financial support from the Helmholtz-OCPC Postdoc-Program from the Helmholtz Association and the Office of China Postdoc Council (Grant No. ZD2019018) and the National Natural Science Foundation of China (Grant No. 52204379). F.N.R. acknowledges support from the Swedish Research Council (Grant No. 2023-04899). N.S.K. acknowledges financial support from the Deutsche Forschungsgemeinschaft through SPP 2137 "Skyrmionics" Grant No. KI 2078/1-1 and BL 444/16-2. F.Z. acknowledges financial support from the Fundamental Research Funds for the Central Universities, the National Natural Science Fund for Excellent Young Scientists Fund Program (Overseas) and for the General Program (Grant No. 52373226), Xiaomi Young Talents Foundation.

Open access funding enabled and organized by Projekt DEAL.

Conflict of Interest

The authors declare no conflict of interest.

Author Contributions

F.Z. and N.S.K. conceived the project and designed the experiments. L.Y. performed the TEM experiments and data analysis. A. S. and N.S.K. performed micromagnetic simulations, with assistance from F.N.R., L.Y., A.S., N.S.K., and F.Z. prepared the manuscript. All of the authors discussed the results and contributed to the final manuscript.

Data Availability Statement

The data that support the findings of this study are available from the corresponding author upon reasonable request.

Keywords

chiral magnet, magnetic imaging, skyrmion, transmission electron microscopy

Received: March 4, 2024
Revised: June 25, 2024
Published online: July 24, 2024

[1] A. M. Kosevich, B. A. Ivanov, A. S. Kovalev, *Phys. Rep.* **1990**, *194*, 117.
[2] Y. Tokura, N. Kanazawa, *Chem. Rev.* **2020**, *121*, 2857.
[3] H. Du, X. Zhao, F. N. Rybakov, A. B. Borisov, S. Wang, J. Tang, C. Jin, C. Wang, W. Wei, N. S. Kiselev, Y. Zhang, R. Che, S. Blügel, M. Tian, *Phys. Rev. Lett.* **2018**, *120*, 197203.
[4] Z. Wang, M. Guo, H.-A. Zhou, L. Zhao, T. Xu, R. Tomasello, H. Bai, Y. Dong, S. G. Je, W. Chao, H.-S. Han, S. Lee, K.-S. Lee, Y. Yao, W. Han, C. Song, H. Wu, M. Carpentieri, G. Finocchio, M.-Y. Im, S.-Z. Lin, W. Jiang, *Nat. Electron.* **2020**, *3*, 672.
[5] X. Yu, F. Kagawa, S. Seki, M. Kubota, J. Masell, F. S. Yasin, K. Nakajima, M. Nakamura, M. Kawasaki, N. Nagaosa, Y. Tokura, *Nat. Commun.* **2021**, *12*, 5079.
[6] G. Qin, X. Zhang, R. Zhang, K. Pei, C. Yang, C. Xu, Y. Zhou, Y. Wu, H. Du, R. Che, *Phys. Rev. B* **2022**, *106*, 024415.
[7] X. Z. Yu, N. Kanazawa, W. Z. Zhang, T. Nagai, T. Hara, K. Kimoto, Y. Matsui, Y. Onose, Y. Tokura, *Nat. Commun.* **2012**, *3*, 988.
[8] W. Wang, D. Song, W. Wei, P. Nan, S. Zhang, B. Ge, M. Tian, J. Zang, H. Du, *Nat. Commun.* **2022**, *13*, 1593.
[9] F. Jonietz, S. Mühlbauer, C. Pfleiderer, A. Neubauer, W. Münzer, A. Bauer, T. Adams, R. Georgii, P. Böni, R. A. Duine, K. Everschor, M. Garst, A. Rosch, *Science* **2010**, *330*, 1648.
[10] K. Everschor-Sitte, J. Masell, R. M. Reeve, M. Kläui, *J. Appl. Phys.* **2018**, *124*, 240901.
[11] B. Göbel, I. Mertig, O. A. Tretiakov, *Phys. Rep.* **2021**, *895*, 1.
[12] M. Birch, D. Cortés-Ortuño, L. A. Turnbull, M. N. Wilson, F. Groß, N. Träger, A. Laurenson, N. Bukin, S. H. Moody, M. Weigand, G. Schütz, H. Popescu, R. Fan, P. Steadman, J. A. T. Verezhak, G. Balakrishnan, J. C. Loudon, A. C. Twitchett-Harrison, O. Hovorka, H. Fangohr, F. Ogrin, J. Gräfe, P. D. Hatton, *Nat. Commun.* **2020**, *11*, 1726.
[13] S. Seki, M. Suzuki, M. Ishibashi, R. Takagi, N. D. Khanh, Y. Shiota, W. Koshibae, Y. Tokura, T. Ono, *Nat. Mater.* **2021**, *21*, 181.
[14] F. Zheng, F. N. Rybakov, N. S. Kiselev, D. Song, A. Kovács, H. Du, S. Blügel, R. E. Dunin-Borkowski, *Nat. Commun.* **2021**, *12*, 5316.
[15] X. Yu, K. V. Iakoubovskii, F. S. Yasin, L. Peng, K. Nakajima, S. Schneider, K. Karube, T. Arima, Y. Taguchi, Y. Tokura, *Nano Lett.* **2022**, *22*, 9358.
[16] S.-T. Hu, *Homotopy Theory*, Academic Press, New York **1959**.
[17] F. Zheng, N. S. Kiselev, F. N. Rybakov, L. Yang, W. Shi, S. Blügel, R. E. Dunin-Borkowski, *Nature* **2023**, *623*, 718.
[18] F. Muckel, S. von Malottki, C. Holl, B. Pestka, M. Pratzer, P. F. Bessarab, S. Heinze, M. Morgenstern, *Nat. Phys.* **2021**, *17*, 395.
[19] I. Dzyaloshinsky, *J. Phys. Chem. Solids* **1958**, *4*, 241.
[20] T. Moriya, *Phys. Rev.* **1960**, *120*, 91.
[21] A. N. Bogdanov, D. A. Yablonskii, *Sov. Phys. JETP* **1989**, *68*, 101.
[22] A. Bogdanov, A. Hubert, *J. Magn. Magn. Mater.* **1999**, *195*, 182.
[23] N. Nagaosa, Y. Tokura, *Nat. Nanotechnol.* **2013**, *8*, 899.
[24] S. Mühlbauer, B. Binz, F. Jonietz, C. Pfleiderer, A. Rosch, A. Neubauer, R. Georgii, P. Böni, *Science* **2009**, *323*, 5916.
[25] F. N. Rybakov, N. S. Kiselev, *Phys. Rev. B* **2019**, *99*, 064437.
[26] D. Foster, C. Kind, P. J. Ackerman, J.-S. B. Tai, M. R. Dennis, I. I. Smalyukh, *Nat. Phys.* **2019**, *15*, 655.
[27] V. M. Kuchkin, B. Barton-Singer, F. N. Rybakov, S. Blügel, B. J. Schroers, N. S. Kiselev, *Phys. Rev. B* **2020**, *102*, 144422.
[28] V. M. Kuchkin, N. S. Kiselev, F. N. Rybakov, P. F. Bessarab, *Front. Phys.* **2023**, *11*, 1171079.
[29] V. M. Kuchkin, K. Chichay, B. Barton-Singer, F. N. Rybakov, S. Blügel, B. J. Schroers, N. S. Kiselev, *Phys. Rev. B* **2021**, *104*, 165116.
[30] C. Kind, D. Foster, *Phys. Rev. B* **2021**, *103*, L100413.
[31] C. Kind, D. Foster, Skyrmionic division, Preprint at arXiv:2207.07337 **2022**.
[32] R. Chen, Y. Li, *ACS Appl. Mater. Interfaces* **2022**, *14*, 30420.
[33] R. Chen, Y. Li, V. F. Pavlidis, C. Moutafis, *Phys. Rev. Res.* **2020**, *2*, 043312.
[34] Z. Zeng, N. Mehmood, Y. Ma, J. Wang, J. Wang, Q. Liu, *J. Phys.: Condens. Matter* **2022**, *34*, 395801.
[35] Z. Zeng, C. Song, J. Wang, Q. Liu, *J. Phys. D: Appl. Phys.* **2022**, *55*, 185001.
[36] L. Bo, R. Zhao, C. Hu, X. Zhang, X. Zhang, M. Mochizuki, *Phys. Rev. B* **2023**, *107*, 224431.
[37] L. Bo, R. Zhao, X. Zhang, M. Mochizuki, X. Zhang, *J. Appl. Phys.* **2024**, *135*, 063905.

© 2024 The Author(s). Advanced Materials published by Wiley-VCH GmbH

15214095, 2024, 36, Downloaded from https://onlinelibrary.wiley.com/doi/10.1002/adma.202403274 by Forschungszentrum Jülich GmbH Research Center, Wiley Online Library on [02/10/2024]. See the Terms and Conditions (https://onlinelibrary.wiley.com/terms-and-conditions) on Wiley Online Library for rules of use; OA articles are governed by the applicable Creative Commons License

[38] S. Li, K.-X. Li, Z.-H. Liu, Q.-Y. Zhu, C.-B. Zhao, H. Zhang, X.-Q. Shi, J.-L. Wang, R.-N. Wang, R.-Q. Lian, P.-L. Gong, C.-D. Jin, *Chin. Phys. B* **2023**, *32*, 117503.
[39] S. Li, J. Liu, Q. Zhu, X. Shi, J. Wang, R. Wang, C. Jin, *Appl. Phys. Lett.* **2024**, *124*, 122403.
[40] X. Bai, J. Wang, J. Yang, Q. Liu, *J. Magn. Magn. Mater.* **2024**, *600*, 172146.
[41] P. Bak, M. H. Jensen, *J. Phys. C* **1980**, *13*, L881.
[42] J. Tang, Y. Wu, W. Wang, L. Kong, B. Lv, W. Wei, J. Zang, M. Tian, H. Du, *Nat. Nanotechnol.* **2021**, *16*, 1086.
[43] Y. Zhang, J. Tang, Y. Wu, M. Shi, X. Xu, S. Wang, M. Tian, H. Du, *Nat. Commun.* **2024**, *15*, 3391.
[44] F. Zheng, H. Li, S. Wang, D. Song, C. Jin, W. Wei, A. Kovács, J. Zang, M. Tian, Y. Zhang, H. Du, R. E. Dunin-Borkowski, *Phys. Rev. Lett.* **2017**, *119*, 197205.
[45] F. Zheng, N. S. Kiselev, L. Yang, V. M. Kuchkin, F. N. Rybakov, S. Blügel, R. E. Dunin-Borkowski, *Nat. Phys.* **2022**, *18*, 863.
[46] L. Powalla, M. T. Birch, K. Litzius, S. Wintz, F. S. Yasin, L. A. Turnbull, F. Schulz, D. A. Mayoh, G. Balakrishnan, M. Weigand, X. Yu, K. Kern, G. Schütz, M. Burghard, *Adv. Mater.* **2023**, *35*, 2208930.
[47] J. Tang, Y. Wu, J. Jiang, L. Kong, S. Wang, M. Tian, H. Du, *Adv. Mater.* **2023**, *35*, 2306117.
[48] A. S. Savchenko, V. M. Kuchkin, F. N. Rybakov, S. Blügel, N. S. Kiselev, *APL Mater.* **2022**, *10*, 071111.
[49] X. Yu, N. Kanazawa, X. Zhang, Y. Takahashi, K. V. Iakoubovskii, K. Nakajima, T. Tanigaki, M. Mochizuki, Y. Tokura, *Adv. Mater.* **2024**, *36*, 2306441.
[50] V. M. Kuchkin, N. S. Kiselev, *Phys. Rev. B* **2020**, *101*, 064408.
[51] H. Du, R. Che, L. Kong, X. Zhao, C. Jin, C. Wang, J. Yang, W. Ning, R. L. C. Jin, X. Chen, J. Zang, Y. Zhang, M. Tian, *Nat. Commun.* **2015**, *6*, 8504.
[52] G. D. Fratta, C. B. Muratov, F. N. Rybakov, V. V. Slastikov, *SIAM J. Math. Anal.* **2020**, *52*, 3580.
[53] F. N. Rybakov, E. Babaev, Excalibur software, http://quantumandclassical.com/excalibur/, (accessed: July 2020).
[54] F. Zheng, F. N. Rybakov, A. B. Borisov, D. Song, S. Wang, Z.-A. Li, H. Du, N. S. Kiselev, J. Caron, A. Kovács, M. Tian, Y. Zhang, S. Blügel, R. E. Dunin-Borkowski, *Nat. Nanotechnol.* **2018**, *13*, 451.
[55] B. Lebech, J. Bernhard, T. Freltoft, *J. Phys.: Condens. Matter.* **1989**, *1*, 6105.
[56] N. Kanazawa, J. S. White, H. M. Rønnow, C. D. Dewhurst, Y. Fujishiro, A. Tsukazaki, Y. Kozuka, M. Kawasaki, M. Ichikawa, F. Kagawa, Y. Tokura, *Phys. Rev. B* **2016**, *94*, 184432.
[57] D. Song, Z.-A. Li, J. Caron, A. Kovács, H. Tian, C. Jin, H. Du, M. Tian, J. Li, J. Zhu, R. E. Dunin-Borkowski, *Phys. Rev. Lett.* **2018**, *120*, 167204.

© 2024 The Author(s). Advanced Materials published by Wiley-VCH GmbH

15214095, 2024, 36, Downloaded from https://onlinelibrary.wiley.com/doi/10.1002/adma.202403274 by Forschungszentrum Jülich GmbH Research Center, Wiley Online Library on [02/10/2024]. See the Terms and Conditions (https://onlinelibrary.wiley.com/terms-and-conditions) on Wiley Online Library for rules of use; OA articles are governed by the applicable Creative Commons License